JOURNAL OF APPLIED CRYSTALLOGRAPHY

ISSN 1600-5767

X-ray free-electron laser based dark-field X-ray microscopy: a simulation-based study

Theodor Secanell Holstad,[a]* Trygve Magnus Ræder,[a] Mads Carlsen,[a] Erik Bergbäck Knudsen,[a] Leora Dresselhaus-Marais,[b,c,d] Kristoffer Haldrup,[a] Hugh Simons,[a] Martin Meedom Nielsen[a] and Henning Friis Poulsen[a]

[a]Department of Physics, Technical University of Denmark (DTU), Fysikvej, Building 311, 2800 Kongens Lyngby, Denmark, [b]Lawrence Livermore National Laboratory, Physics Division, 7000 East Avenue, Livermore, CA 94550, USA, [c]Stanford University, Department of Materials Science and Engineering, 476 Lomita Mall, Stanford, CA 94305, USA, and [d]SLAC National Accelerator Laboratory, 2575 Sand Hill Road, Menlo Park, CA 94025, USA. *Correspondence e-mail: theol@dtu.dk

Received 22 October 2021
Accepted 30 November 2021

Edited by S. Boutet, SLAC National Accelerator Laboratory, Menlo Park, USA

Keywords: dark-field X-ray microscopy; X-ray free-electron lasers; strain waves; phonons; dynamics.

Supporting information: this article has supporting information at journals.iucr.org/j

Dark-field X-ray microscopy (DFXM) is a nondestructive full-field imaging technique providing three-dimensional mapping of microstructure and local strain fields in deeply embedded crystalline elements. This is achieved by placing an objective lens in the diffracted beam, giving a magnified projection image. So far, the method has been applied with a time resolution of milliseconds to hours. In this work, the feasibility of DFXM at the picosecond time scale using an X-ray free-electron laser source and a pump–probe scheme is considered. Thermomechanical strain-wave simulations are combined with geometrical optics and wavefront propagation optics to simulate DFXM images of phonon dynamics in a diamond single crystal. Using the specifications of the XCS instrument at the Linac Coherent Light Source as an example results in simulated DFXM images clearly showing the propagation of a strain wave.

1. Introduction

During the past decade, dark-field X-ray microscopy (DFXM) has emerged as a tool for mapping the microstructure within bulk crystalline materials in three dimensions (Simons *et al.*, 2016; Kutsal *et al.*, 2019; Yildirim *et al.*, 2020). Using an objective lens to magnify Bragg-diffracted high-energy X-rays, DFXM facilitates mapping of orientation (with a sensitivity of 0.1 mrad) and strain (sensitivity of 10^{-4} to 10^{-5}) in deeply embedded structures with a spatial resolution down to 30–100 nm (Poulsen *et al.*, 2017, 2018; Kutsal *et al.*, 2019). This technique has been applied to characterize, for example, grain structure and dislocation networks in metals (Simons *et al.*, 2015, 2016; Jakobsen *et al.*, 2019; Dresselhaus-Marais *et al.*, 2021), dislocation toughening of ceramics (Porz *et al.*, 2021), and ferroelectric domains and domain walls (Simons *et al.*, 2016, 2018; Schultheiß *et al.*, 2021). So far, DFXM has been applied at synchrotrons, with a time resolution of about 100 ms. On the one hand, this is sufficient to image some dynamic processes *in situ*, such as recovery in metals (Yildirim *et al.*, 2020), dislocation motion close to the melting point in aluminium (Gonzalez *et al.*, 2020; Dresselhaus-Marais *et al.*, 2021), and structural transformations taking place in ferroelectrics during phase transitions (Ormstrup *et al.*, 2020) or mechanical loading. While DFXM was recently demonstrated at an X-ray free-electron laser (XFEL), its time resolution measuring X-ray damage was still limited to 33 ms by the repetition rate of the source (Dresselhaus-Cooper, 2020). On the other hand, other dynamic processes, such as phonon

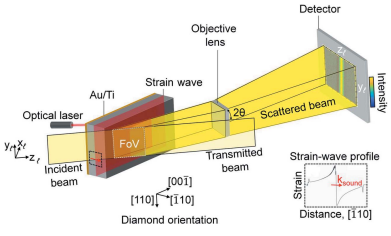

propagation, occur on much shorter picosecond timescales. Up to now, imaging of phonon waves has been limited to thin specimens ($\lesssim 50$ nm) using dark-field transmission electron microscopy (Cremons *et al.*, 2016), to nanocrystals using Bragg coherent diffraction imaging (Clark *et al.*, 2013; Wen *et al.*, 2019) and to THz imaging (Ofori-Okai *et al.*, 2014).

An optical-laser-pump–X-ray-probe scheme has previously been applied to study phonon dynamics using diffraction methods at XFELs, where the enhanced brightness and pulse duration allow for the finer time resolutions necessary to study phonon dynamics (Lindenberg *et al.*, 2000; Larsson *et al.*, 2002; Persson *et al.*, 2015; Jarnac *et al.*, 2017; Lemke *et al.*, 2018). Here, we propose to implement DFXM at an XFEL using such a pump–probe scheme. This will allow direct visualization of the interaction between sound waves and microstructural features such as domain walls or dislocations deep within millimetre-sized single- and polycrystalline materials – of interest to materials physics, seismology and extreme condensed matter science.

In this work, we provide a numerical demonstration of the feasibility of this scheme. We simulate longitudinal sound-wave propagation in a diamond single crystal using the thermomechanical Python modeling package *udkm1Dsim* (Schick *et al.*, 2014; Schick, 2021). Forward simulations of DFXM data are performed using both geometrical optics (Poulsen *et al.*, 2021) and wavefront propagation optics (Carlsen & Simons, 2021) to explore the DFXM parameter space and optimize the experimental configuration. Using a setup relevant for an experiment at the XCS instrument at the Linac Coherent Light Source (LCLS) as an example, the simulations show the propagation of a longitudinal strain wave with both a clear contrast and a good signal-to-noise ratio from a single pulse, thereby opening the door to investigating the materials science entailed in dynamic imaging of phonon propagation (Wolfe & Hauser, 1995; Siemens *et al.*, 2010; Hatanaka *et al.*, 2014). Moreover, we demonstrate how geometrical aspects of this experiment may be optimized to improve contrast.

2. Experimental

2.1. DFXM geometry and contrast

The methodology of DFXM in general and associated properties such as spatial and reciprocal-space resolution are presented in detail elsewhere (Poulsen *et al.*, 2017, 2018, 2021).

The DFXM geometry considered in this work is illustrated in Fig. 1.[1] A nearly monochromatic X-ray beam with wavelength λ is condensed in the horizontal direction to generate a vertical line beam focused onto the sample; this defines a vertical plane of observation inside the sample. The incident beam is defined by its vertical width (*i.e.* height) Δy, its horizontal thickness Δx and its horizontal divergence $\Delta\zeta_{\rm h}$.

The sample is mounted on a goniometer designed to access diffraction angles in a horizontal scattering geometry and probe reciprocal space in the immediate vicinity of a given reflection $\mathbf{Q}_0$, corresponding to lattice planes $(hk\ell)$. The implementation considered here achieves this by moving the sample along a combination of ω, χ and ϕ rotation stages [see Fig. 1(*b*)]. The direction of the diffracted beam in the horizontal plane is characterized by the scattering angle, $2\theta_0$ (for the nominal $hk\ell$ reflection). The motor position in the horizontal plane is denoted as 2θ (Fig. 1). We shall assume that the motor position is exactly at the scattering angle, *i.e.* that $2\theta = 2\theta_0$. The optical axis of an X-ray objective lies along the diffracted beam for $\mathbf{Q}_0$ to produce a magnified and inverted image of the illuminated plane on the 2D detector. As is usually used for DFXM experiments, we assume a compound refractive lens (CRL) objective for this simulation (Snigirev *et al.*, 1996), which is a thick lens comprising N identical parabolic lenslets (Simons *et al.*, 2017). The CRL is characterized by a numerical aperture NA and a focal length $f_{\rm N}$. The image generated by the objective has an associated magnification ($\mathcal{M}$) and field of view (FoV) in the object plane (*i.e.* the crystalline sample). The projection angle implies that the illuminated plane is observed at an angle with a resulting aspect ratio of 1:tan(2θ).

The relations between reciprocal space and strain components and between micro-mechanical models and DFXM images are discussed in detail by Poulsen *et al.* (2021). The vicinity of $\mathbf{Q}_0$ in reciprocal space can be probed in three orthogonal directions by scanning ϕ, χ, and a combination of ϕ

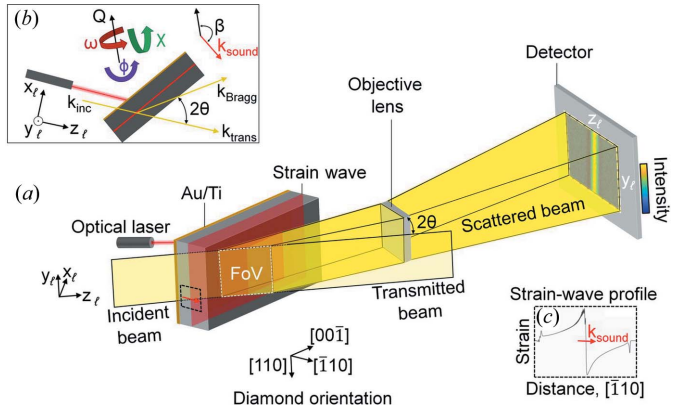

Figure 1
(*a*) Schematic of the configuration for pump–probe DFXM imaging of a strain wave used for the simulations. A crystallographic coordinate system indicates the diamond orientation. An optical laser (pump) heats a deposited Au film. This leads to thermal expansion and the launching of a strain wave (red plane) into the diamond. An incident X-ray beam (probe) is condensed into a sheet which penetrates the diamond crystal at some time delay after the laser excitation. A laboratory coordinate system (x_ℓ, y_ℓ, z_ℓ) is defined with x_ℓ, y_ℓ and z_ℓ parallel to the incident beam width, height and propagation direction, respectively. The diamond crystal is oriented such that the {111} planes Bragg scatter, and an objective lens is positioned in the Bragg-scattered beam. This results in a magnified image of a field of view (FoV) (white dashed lines) being projected onto the detector. The colorscale shows the photon count in a simulated image (see Section 3.2). (*b*) The upper-left inset shows a top-down view of the setup. We assume the sample is mounted on a goniometer which can perform an ω rotation around the local diffraction vector $\mathbf{Q}$ and two orthogonal tilts, χ and ϕ. The angle β between the wavevector of the strain wave $\mathbf{k}_{\rm sound}$ and the diffraction vector $\mathbf{Q}$ is indicated. (*c*) The simulated 1D strain-wave profile (see Section 3.1) is shown in the inset with dark dashed lines.

[1] Note that in the XFEL community the optical axis is along $\mathbf{z}_\ell$, whereas in the DFXM community it typically is along $\mathbf{x}_\ell$.

and 2θ, respectively. These are referred to as rocking, rolling (both of which probe the local mosaicity) and longitudinal strain scans, respectively, and may be combined. The contrast in the resulting images scales according to the local values of three of the displacement gradient tensor field elements. The longitudinal ϕ–2θ scan corresponds to probing the axial strain along the diffraction vector $\mathbf{Q}_0$. For a material with no rotation of the lattice planes, the other two scans represent shear strains.

2.2. Dynamic strain-wave characterization

The aim of this article is to provide insight into how to design and optimize an optical-laser-pump–X-ray-probe DFXM experiment at an XFEL with the aim of imaging strain-wave movement. At XFELs, a single pulse typically has a duration of 1–100 fs (Inoue *et al.*, 2019). Provided the contrast and signal-to-noise ratio are suitable, one may then image the structure and strain in the illuminated layer, averaged over this time interval. Here, we focus on reversible processes that are suitable for a pump–probe scheme. Specifically, we consider the visualization of an isolated longitudinal sound wave traversing a single crystal. With sound speeds of 18 km s^{-1} (Wang *et al.*, 2004), the strain wave will travel 18 pm–1.8 nm within the duration of the pulse, much less than the spatial resolution, meaning that no temporal blurring needs to be considered in the image.

The longitudinal sound wave will give rise to one strain component ε in the direction of its propagation, $\mathbf{k}_{\rm sound}$. Let β be the angle between $\mathbf{Q}_0$ and $\mathbf{k}_{\rm sound}$ (Fig. 1). Then, the projection $\varepsilon\cos(\beta)$ is probed in the DFXM experiment. Depending on the goniometer setting, the projected strain can be visualized in several ways, including the 'strong-beam' and 'weak-beam' conditions (Jakobsen *et al.*, 2019) to be explored below.

2.3. Simulation parameters

To determine the feasibility of visualizing sound waves we shall consider propagation of such a wave in single-crystal diamond with an experimental setup that is relevant to the XCS instrument at the LCLS. That instrument is well suited for DFXM as it is equipped with a long arm (8 m) that is rotated radially about a sample's diffraction 2θ angles. The layout of such an experiment is shown in Fig. 1. To ensure that the results of the numerical simulations will reflect future experimental realities, we describe in detail the parameters that are considered typical of this beamline.

The diamond single crystal is specified to have dimensions of $0.6 \times 1 \times 2$ mm with $(1\bar{1}0)$, (110) and (001) facets. The $(1\bar{1}0)$ facet is coated with a 15 nm Ti adhesion layer followed by a 600 nm Au layer, which thermalizes when irradiated optically. We shall assume a width of the diamond sample rocking curve of $\Delta_{\rm mosaic} = 200$ µrad. The Au layer is excited with a 100 fs laser pulse ($\lambda = 800$ nm; fluence = 0.8 J cm^{-2}). The subsequent impulsive expansion of the Au film results in strain waves propagating from the Au film and into the diamond crystal (see Section 3.1 below).

The XFEL pulses are assumed to be 10 keV, with a pulse duration of 35 fs and energy of 2 mJ. These are monochromated to give an energy band width (FWHM) of $\Delta E/E \simeq 10^{-4}$ and a divergence of approximately 1.1×1.1 µrad after the monochromator. Before the beam hits the sample, it is condensed by a set of 1D Be lenses into a line beam (Fig. 1) with a vertical width $\Delta y = 500$ µm, a horizontal thickness (FWHM) $\Delta x = 3$ µm and a horizontal divergence (FWHM) $\Delta\zeta_{\rm h} = 30$ µrad. The 10^{-4} bandwidth of the monochromator and the significant width, intra-pulse substructure due to microbunching and shot-to-shot variation in $I(E)$ in combination with absorption loses in the lens system mean that the average photon count after the monochromator can be expected to be reduced to $N_{\rm estimated,\,inc} = 2 \times 10^{10}$ photons per pulse incident on the sample. As such, this is the average photon count used in the simulations below, but we note that significant shot-to-shot variation in photon count (from 0 to 10^{12} photons per pulse) is expected in an actual XFEL experiment.

The incoming X-ray sheet slices through the crystal, and the X-rays that are Bragg-scattered from {111} planes ($2\theta_0 = 35.04^\circ$) are projected by the objective lens stack onto a 2D detector at a fixed position $L = 7.1$ m downstream from the sample. The objective is a CRL with $N = 30$ Be lenslets, each with a radius of curvature of $R = 50$ µm, a distance between centers of neighboring lenslets of $T = 2$ mm, and a thickness of each lenslet of $T_{\rm effective} = 1$ mm. Using the analytical expressions of Simons *et al.* (2017), the corresponding effective focal length is $f_{\rm N} = 0.207$ m, the sample-to-objective-entry-plane distance $d_1 = 0.215$ m, the objective-to-detector distance $d_2 = 6.83$ m, the effective numerical aperture (FWHM) NA = 0.000845, the physical aperture 447 µm and the magnification of the X-ray objective $\mathcal{M} = 27.9$. The CMOS detector at the beamline is assumed to have a pixel size of 6.5×6.5 µm and 2560×2160 pixels. In the simulation below we assume a 1:1 coupling between the scintillator screen and the camera, and $2\times$ binning. The effective pixel size in the observation plane (the intersection between the incident beam and the crystal) is then 466×664 nm.

3. Modeling

The full DFXM phonon modeling begins with the thermo-mechanical model of the light–matter interaction and associated phonon wavepacket in the sample, *i.e.* the strain wave. The resulting micro-mechanical model is then used as the input for forward models of the DFXM images as function of $(\phi, \chi, 2\theta)$ and of the orientation of the single crystal. The parameters of the experimental configuration presented in Section 2.3 are used throughout.

3.1. Strain-wave modeling

A laser is used to heat an Au film deposited on a diamond crystal (see Section 2.3 for details). A one-dimensional thermomechanical model, *udkm1Dsim* (Schick *et al.*, 2014; Schick, 2021), is utilized to compute the propagation of the resulting

strain wave in the propagation direction, z_{sw}. This model has previously been successfully implemented to simulate strain-wave propagation in a gold-coated indium antimonide crystal (Jarnac *et al.*, 2017).

The *udkm1Dsim* Python package uses the two-temperature model (Jiang & Tsai, 2005; Tzou *et al.*, 2002), where the electrons and crystal lattice have separate temperatures and heat diffusion equations, to compute the temperature distribution after the laser excitation. For the electrons, the heat diffusion equation is

$$C_e(T_e)\frac{\partial T_e}{\partial t} = \frac{\partial}{\partial z_{sw}}\left[k_e(T_e, T_l)\frac{\partial T_e}{\partial z_{sw}}\right] + G_e(T_e, T_l) + S(z_{sw}, t). \quad (1)$$

Here, T_e is the electronic temperature, T_l is the crystal lattice temperature, C_e is the heat capacity of the electrons and k_e is the thermal conductivity of the electrons. $S(z_{sw}, t)$ is the source term which describes absorption of the laser energy by the electrons [see the article by Schick *et al.* (2014) for details], and G_e is the lattice–electron coupling factor.

The corresponding heat diffusion equation for the crystal lattice (l) is

$$C_l(T_l)\frac{\partial T_l}{\partial t} = \frac{\partial}{\partial z_{sw}}\left[k_l(T_l)\frac{\partial T_l}{\partial z_{sw}}\right] + G_l(T_e, T_l). \quad (2)$$

The crystal lattice heat capacity C_l and thermal conductivity k_l are temperature independent, while the temperature dependence of the electronic heat capacity and thermal conductivity are given by (Tzou *et al.*, 2002)

$$C_e(T_e) = C_{e0}(T_e/T_0) \quad (3)$$

and

$$k_e(T_e, T_l) = k_{e0}(T_e/T_l), \quad (4)$$

respectively. Here T_0 is the initial temperature (300 K) and the subscript e0 refers to the respective initial values for the electrons.

The electron–lattice coupling terms in the diffusion equations are taken to be proportional to the difference between the electronic and lattice temperatures (Tzou *et al.*, 2002; Jiang & Tsai, 2005; Schick *et al.*, 2014; Jarnac *et al.*, 2017; Schick, 2021):

$$G_l(T_e, T_l) = G(T_e - T_l), \quad (5)$$

$$G_e(T_e, T_l) = G(T_l - T_e). \quad (6)$$

The proportionality factor G is also temperature dependent (Jiang & Tsai, 2005; Lin *et al.*, 2008), and the temperature dependencies used in the present simulations are taken from the article by Lin *et al.* (2008).

Solving the heat diffusion equations (1) and (2) gives a temperature profile at different time delays after the laser excitation. The linear thermal expansion coefficient of the crystal lattice (α in Table 1) is then used to compute the thermal expansion. Subsequently, a model composed of a linear chain of point masses connected by springs is used to compute the resulting crystal lattice dynamics of the longitudinal strain waves [Schick *et al.* (2014) provide further details].

Table 1
Parameters used in strain-wave simulations.

Properties	Gold	Ti	Diamond
k_{e0} (W m^{-1} K^{-1})	315[a]	10[b]	0
k_l (W m^{-1} K^{-1})	2.6[c]	10[b]	1200[d]
C_{e0} (J m^{-3} K^{-1})	2.1×10^{4} [a]	328.9[e]	0
C_l (J m^{-3} K^{-1})	2.5×10^{6} [a]	2.21×10^{6} [f]	[g]
G (W m^{-3} K^{-1})	[e]	[e]	[e]
c_s (nm ps^{-1})	3.24[h]	6.16[i]	18[j]
α (K^{-1}) $\times 10^{6}$	13.99[k]	8.5[l]	1.06[m]
ρ (g cm^{-3})	19.3	4.506	3.51[n]

References: (*a*) Tzou *et al.* (2002); (*b*) Klemens & Williams (1986); (*c*) Wang *et al.* (2016); (*d*) Anthony *et al.* (1990); (*e*) Lin *et al.* (2008); (*f*) Victor (1962); (*g*) Rao & Rajput (1979); (*h*) Ismail *et al.* (2018); (*i*) Zaretsky (2008); (*j*) Wang *et al.* (2004); (*k*) Dutta & Dayal (1963); (*l*) Hidnert (1943); (*m*) Jacobson & Stoupin (2019); (*n*) Graebner (1996).

3.2. DFXM forward modeling

In the following, we consider DFXM imaging based on the most intense reflection $\mathbf{Q}_0 = \langle 111 \rangle$. Moreover, we will assume that the propagation direction of the sound wave, $\mathbf{k}_{sound}$, is in the scattering plane at an angle β to $\mathbf{Q}_0$ (Fig. 1).

3.2.1. Geometrical-optics formalism. A formalism for forward simulation of DFXM images based on geometrical optics is described by Poulsen *et al.* (2021). The input is a voxelized version of a displacement gradient tensor field – which in our case is readily provided by the 1D strain-wave model above. The forward simulation is based on analytical expressions for the relation between strain, reciprocal space and the resulting detector intensity distribution. The instrumental resolution function is determined by Monte Carlo simulations prior to the actual forward simulations. This means that the method is relatively fast and well suited for optimization purposes. On the other hand, geometrical optics is not inherently suited for studying effects such as coherence and in particular dynamical diffraction, which may be relevant for DFXM studies of single crystals.

The simulations below were performed by a slightly revised version of the code provided as supplementary information by Poulsen *et al.* (2021), which also now takes into account counting noise. This is based on a model of the counts per pixel for the strain-free single crystal in the optimized 'strong-beam' condition, the latter term meaning that the crystal's orientation with respect to the incident beam is centered on the Bragg condition, *i.e.* the strongest part of the rocking curve ($\phi = \chi = 0, 2\theta = 2\theta_0$). Specifically, the diffracted photon count for one pulse as summed over the image for the strong-beam setting is estimated as follows:

$$N_{estimated,strong} = N_{estimated,inc}\frac{A_{FoV}}{A_{ill}}T\frac{\Delta_{Darwin}}{\Delta_{mosaic}}\frac{1}{2}. \quad (7)$$

Here, $N_{estimated,inc}$ is the estimated total number of photons incident on the sample, A_{FoV} is the area of the field of view in the illuminated plane and A_{ill} is the total area of the

illuminated plane within the diamond crystal: $A_{\rm ill} = \Delta y\, b/\sin[\angle(k_{\rm inc}, \text{crystal surface})]$, where $[\angle(k_{\rm inc}, \text{crystal surface})]$ is the grazing angle between the incident X-ray beam and the diamond crystal's surface and b is the thickness of the diamond crystal along the direction perpendicular to the gold-coated facet. T is the average transmission through Au and diamond, and $\Delta_{\rm Darwin}$ is the Darwin width, which for diamond(111) and 10 keV is 20 µrad. $\Delta_{\rm Darwin}/\Delta_{\rm mosaic}$ is a rough approximation for the ratio of the sample diffracting dynamically, and the factor $\frac{1}{2}$ expresses that, in this regime, the average photon count is equally distributed between the transmitted and Bragg-scattered beams. We will in the simulations below work with a region of interest of $M \times M = 100 \times 100$ binned pixels.

Next, a simulated value of the strong-beam photon count is calculated for the strain-free single crystal, $N_{\rm simulated,strong}$. The number of photons detected in each pixel is then determined by sampling from a Poisson distribution with the mean given by the pixel values in raw simulated images, $N_{\rm simulated,raw}(i, j)$ [following Poulsen *et al.* (2021)], scaled by the ratio of the estimated to the simulated strong-beam value for the diffracted photon count:

$$N_{\rm abs}(i, j) \in \text{Pois}\left[\frac{N_{\rm estimated,strong}}{N_{\rm simulated,strong}} N_{\rm simulated,raw}(i, j)\right]. \quad (8)$$

The scaling factor in equation (8) relates the raw photon count of the simulated image $N_{\rm simulated,raw}$ to the photon count estimated in equation (7). This scaling is valid for each pixel, because in a strain-free single crystal the image is homogeneous and the diffracted photon count per pixel is $N_{\rm total}/M^2$, where M^2 is the total number of pixels. This scaling is also used for the 'weak-beam' conditions – where the orientation of the crystal with respect to the incident beam is just at the edge of the Bragg condition, *i.e.* the weakest part of the rocking-curve – because the simulations internally scale weak- and strong-beam conditions correctly. We note that this procedure does not take any non-ideal effects of the detector into account. It merely yields a realistic estimate of the signal arriving at the detector plane. The noise model is included as supplementary information.

3.2.2. Wave-optics formalism. The wave-optics simulations represent linearly polarized X-rays as a coherent wavefront of an electric field with the complex-valued amplitude given on a discrete two-dimensional grid. The electric field throughout the crystal is simulted as two components, one propagating along the incident beam and one propagating in the scattered beam direction. Scattering is handled by the transfer of amplitude between the incident and scattered electric field, with scaling based on the electron density of the deformed crystal structure in each voxel [$\simeq$ structure factor of (h, k, ℓ) and $(\bar{h}, \bar{k}, \bar{\ell})$] in the formalism of the Takagi–Taupin equations defined by Takagi (1962). The Takagi–Taupin formalism allows for multiple scattering events, *i.e.* dynamical diffraction, where each scattering event introduces a 90° phase shift. The images in the strong-beam condition are dominated by the '*Pendellösung* fringes' that arise from multiple scattering events, as intensity beats between the direct and the scattered beam (*i.e.* interference effects from the phase shift introduced by the scattering). The wave-optics formalism therefore allows us to investigate the strong-beam condition, as well as verifying that offsetting the sample by rotating the goniometer in ϕ yields only weak-beam contrast, with negligible contribution from dynamical diffraction.

The Takagi–Taupin equations are numerically integrated using the method given by Carlsen & Simons (2021). The scattered field is propagated through the CRL and to the detector using Fourier propagation methods described by Pedersen *et al.* (2018). A 3D grid of 16000 × 1200 × 8000 voxels is used, with a voxel size of 125 × 62.5 × 62.5 nm along the $[00\bar{1}]$, [110] and $[\bar{1}10]$ directions, respectively. The full size of the diamond crystal along $[00\bar{1}]$ and $[\bar{1}10]$ is simulated in order to correctly capture the fringes caused by dynamical diffraction, but we do not simulate the full size of the crystal along [110], as the crystal is taller than the FoV. A Gauss–Schell beam is used, which is a quasi-monochromatic beam that has a Gaussian profile in both real and reciprocal space represented by a series of (independently coherent) modes. The majority of the intensity is contained in the first mode (a

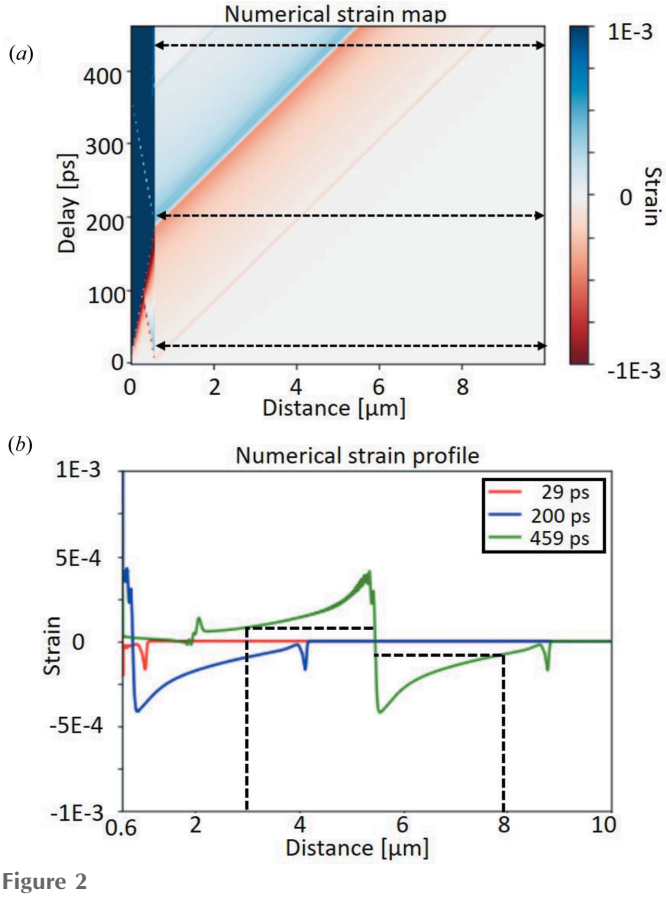

Figure 2
Strain-wave profile in a diamond single crystal as a function of time delay from laser pulse heating, as computed using a 1D thermomechanical model. (*a*) 2D map of strain versus depth and time delay. (*b*) 1D plots of the strain profile in diamond at different time delays [indicated with dashed lines in (*a*)]. The spatial extent of the part of the strain wave that is visible in DFXM at 459 ps (indicated with dashed lines) is about 5 µm.

largely coherent beam), and only four modes are included. The parameters of the Gauss–Schell beam are $\sigma_I = 1.7$ µm and $\sigma_c = 1.2$ µm as defined by Starikov & Wolf (1982).

4. Results

4.1. Strain-wave simulation results

Fig. 2(*a*) displays the strain profile with distance and time on the horizontal and vertical axes, respectively. Fig. 2(*b*) shows the strain inside the diamond crystal as a function of distance from the gold film, with different colors showing different time delays.

The traces furthest from the surface (*i.e.* later in time delay) demonstrate that the strain profile is anti-symmetric around the 'position' of the strain pulse with a maximum strain that is approximately 4×10^{-4}. Given the strain resolution of DFXM, the spatial extent of the visible part of the strain wave is about 5 µm [see Fig. 2(*b*)]. In diamond, the wave travels 6.3 Å during the LCLS XFEL pulse duration (35 fs), which is much smaller than the spatial resolution and thus negligible.

4.2. DFXM simulation results

4.2.1. Geometrical-optics formalism. From the experimental geometry introduced above, the resolution as expressed in terms of how a single point in q space is broadened due to finite NAs *etc.* can be estimated. This broadening is referred to as the 'reciprocal-space resolution function', and Fig. 3 shows this based on Monte Carlo modeling of 10 000 simulated rays propagating through the optical system for the $\phi = \chi = 0$ and $2\theta = 2\theta_0$ scattering geometry.[2] The Monte Carlo ray simulation is visualized in a $(q_{\mathrm{rock}'}, q_{\mathrm{roll}}, q_{2\theta})$ coordinate system, which is referred to as the 'imaging coordinate system' by Poulsen *et al.* (2021). It is rotated with respect to the laboratory system shown in Fig. 1 by 2θ around the y_ℓ axis.

The 3D resolution function (blue) in Fig. 3 is projected onto the three possible q-space planes to demonstrate the intrinsic anisotropy, which is significantly more dramatic than is observed for synchrotron experiments (Poulsen *et al.*, 2021). Comparison of the projection shown in orange with those in yellow and purple shows a large anisotropy in the reciprocal-space resolution function. To first order, the resolution function is a disc, with a 'thin dimension' parallel to the optical axis of the objective. The width (FWHM) of this is below 10^{-4}. The dimensions of the two wide axes are defined by the acceptance functions set by the NA of the objective lens, producing a nearly planar distribution. The width in the $q_{\mathrm{rock}'}$ direction is largely determined by the horizontal divergence of the incident radiation, *i.e.* the NA of the condenser lens, and is not the result of a more coherent source.

The majority of the crystal is strain free and will therefore give rise to diffraction at the setting where $\mathbf{Q} = \mathbf{Q}_0$. The sound wave may be visible in this strong-beam condition, but dynamical diffraction makes it difficult to quantify and interpret such images, and in any case such contrast cannot readily be simulated by geometrical optics.

By rotating the sample in ϕ – rocking the sample – by an amount $\Delta\phi$, which is larger than the thin dimension of the resolution function (moving along $q_{\mathrm{rock}'}$ in Fig. 3), dynamical scattering from the unstrained part of the crystal is avoided because it no longer satisfies the Bragg condition. Such a movement corresponds to a shear strain of magnitude $\Delta\phi$. Likewise, by rotating the sample in χ – rolling the sample (moving along q_{roll} in Fig. 3) – by an amount $\Delta\chi$, which is larger than $\mathrm{NA}/[2\sin(\theta)]$, dynamical scattering from the unstrained part of the crystal is avoided, and we have another type of weak-beam contrast. Such a movement corresponds to a shear strain of magnitude $\Delta\chi$ (Poulsen *et al.*, 2017).

Finally, by offsetting the crystal in 2θ by an amount $\Delta 2\theta$ larger than NA – and a simultaneous offset in ϕ – weak-beam contrast is obtained in the longitudinal direction (moving along $q_{2\theta}$ in Fig. 3). In this case the movement corresponds to an axial strain of magnitude $\Delta 2\theta/[2\tan(\theta)]$ (Poulsen *et al.*, 2017).

From the resolution function in Fig. 3, we anticipate to resolve the sound wave in more detail when weak-beam contrast can be obtained by rocking the sample (because the resolution function is narrow along $q_{\mathrm{rock}'}$). For rolling and longitudinal strain scans we note that the diameter of the disc in reciprocal space nearly matches the full range of the strain field. For this reason, it is difficult to reach weak-beam contrast for such scans. Instead it may be relevant to operate in a strong-beam contrast mode, where the contrast is reversed.

We have forward simulated DFXM images of the strain-wave propagation for a number of angles β. In Fig. 4, we present snapshots for β = 180, 144.74 and 54.74°, corresponding to the strain wave propagating along $[\bar{1}11]$, $[\bar{1}10]$ and $[00\bar{1}]$, respectively. Note that Fig. 4(*a*) corresponds to a diamond with different facets and Fig. 4(*c*) to a diamond with different shape compared with the one shown in Fig. 1. We demonstrate the use of two types of contrast: rocking-type weak-beam contrast and rolling-type strong-beam contrast. Suitable offsets were identified by inspection to be

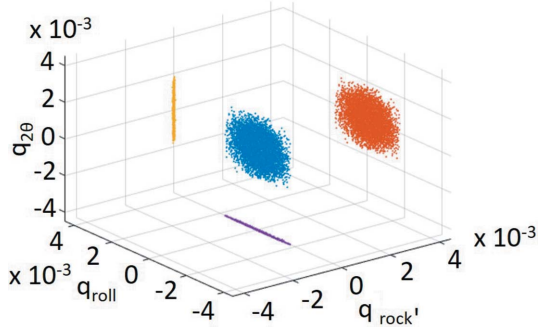

Figure 3
Reciprocal-space resolution function for the simulated DFXM setup. The simulation involved 10 000 simulated rays. Blue symbols: 3D scatter plot for the resolution function expressed in a coordinate system collinear with the image plane. The purple, orange and yellow symbols correspond to 2D projections onto the $q_{\mathrm{rock}'}q_{\mathrm{roll}}$ plane, $q_{\mathrm{roll}}q_{2\theta}$ plane and $q_{\mathrm{rock}'}q_{2\theta}$ plane, respectively.

[2] Strictly speaking, the simulation is only valid for a sample position which is on the optical axis of the objective, as discussed by Poulsen *et al.* (2021), who also present expressions for the general case.

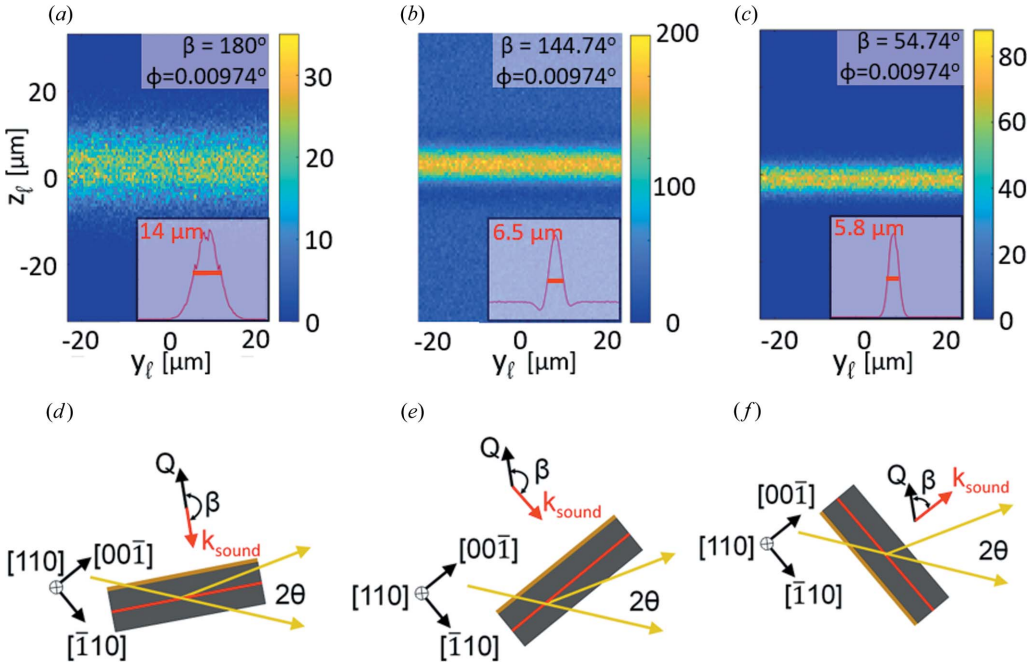

Figure 4
Single-pulse DFXM images simulated using geometrical optics at the time when the sound wave is centered within the FoV. The three rows plot cases in which the experiment is set up with angles between the diffraction vector and sound propagation direction of (*a*) $\beta = 180°$, (*b*) $\beta = 144.74°$ and (*c*) $\beta = 54.74°$ (corresponding to sound waves propagating along [$\bar{1}$11], [$\bar{1}$10] and [00$\bar{1}$], respectively), as indicated schematically in the bottom row (*d*)–(*f*). All DFXM images have an orientational offset in the rocking direction ϕ to achieve weak-beam contrast. The pixel size in the object plane (intersection between incident beam and crystal, *i.e.* the 'gauge volume') is 466 × 664 nm. The colorbar denotes the number of detected photons per pixel, without corrections for quantum efficiency or other detector effects. The insets are integrated photon-count profiles along the $\mathbf{z}_\ell$ direction, and the FWHM is indicated in red.

$\Delta\phi = 0.00974°$ and $\Delta\chi = 0.0974°$, respectively. Corresponding movies of the entire ϕ and χ scans are available as supplementary material.

The ϕ scans show strong contrast in the weak-beam condition, with pixel intensity differentials across the strain wave as high as 200 counts. For all β cases, weak-beam contrast appears in the images when the offset in ϕ is in the range between the maximum strain, 4×10^{-4} rad, and the width of the reciprocal-space resolution function in direction ϕ (*cf.* Fig. 3).

The variations with β are readily explained. For $\beta = 180°$, the planar wavefront is more parallel to the observation plane in the crystal, leading to a wider and consequently less intense signal [Fig. 4(*a*)]. The images in Figs. 4(*b*) and 4(*c*) plot DFXM for $\beta = 144.74°$ and $\beta = 54.74°$, showing a compromise between having the wavefront perpendicular to the observation plane, which makes the wave appear more narrow, and maximizing the projected strain signal given by $\varepsilon\cos(\beta)$, *i.e.* the signal that DFXM measures.

The contrast exhibited in the χ scans is less pronounced. As already discussed, the applicability of geometrical optics for strong-beam conditions is questionable, making this scan geometry better described using the wave-optics formalism, as discussed in the next section.

4.2.2. Wave-optics formalism. Results from the wave-optics simulations are shown in Fig. 5. These simulations are constructed with the strain profile in Fig. 2(*a*) propagating along the [$\bar{1}$10] direction [$\beta = 144.74°$; see Figs. 1 and 4(*e*)]. As in the previous example, we plot the strain wave at a time when it is at the center of the FoV. Fig. 5(*a*) gives a realistic view of the strong-beam condition, in which we account for dynamical diffraction that causes the strain wave to appear blurred.

In the strong-beam condition, the bulk shows low intensity as the low-frequency Fourier components (corresponding to

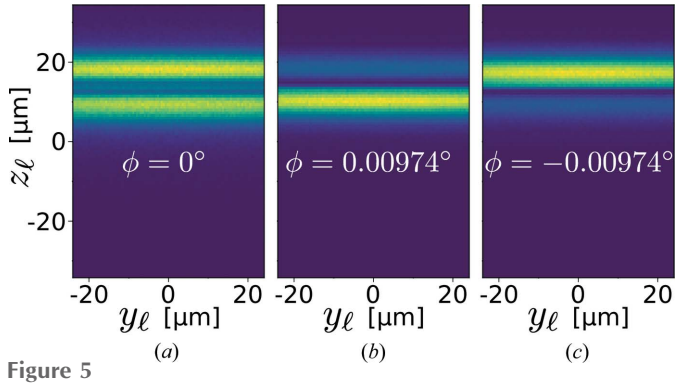

Figure 5
Results from wave-optics simulations in the strong-beam condition (*a*), and in the ϕ-type weak-beam condition from rocking in a positive (*b*) and negative (*c*) direction. All simulations are done with the sound waves propagating along the [$\bar{1}$10] direction ($\beta = 144.74°$), and using the strain profile shown in Fig. 2 translated to the center of the crystal. The intensity is shown with arbitrary units.

the rays at a low divergence angle) of the incoming beam are multiply scattered and spread across the entire FoV. The defect, on the other hand, scatters the high-frequency components of the beam, which are unlikely to scatter again, and thus appears brighter. The FoV of this image is taken from the center of the crystal, where the periodicity of the *Pendellösung* fringes (from dynamical scattering) is larger than the FoV and appears as a constant background. The intensity of the *Pendellösung* fringes is much smaller than the intensity generated by the strain wave, but may provide a challenge to imaging if the strain wave has a smaller amplitude.

To get from Fig. 5(*a*) to Figs. 5(*b*) and 5(c), the sample is rocked into the ϕ-type weak-beam condition, causing the strain wave to appear as a much more clearly defined object in the DFXM images. This can be rationalized by considering the contrast mechanisms in the two cases. When the sample is rocked, the crystal is rotated out of the Bragg condition while the strain wave introduces a longitudinal distortion which both elongates and rotates the scattering vector. This rotation brings the highly strained center of the strain wave closer to the Bragg condition than the surrounding crystal. Specifically, a positive ϕ brings the compressive part of the strain wave closer to the Bragg condition [Fig. 5(*b*)], while a negative ϕ will bring the tensile part of the strain wave closer to the Bragg condition [Fig. 5(*c*)].

5. Discussion and outlook

The above simulations demonstrate (i) that we can generate strain waves in diamond by using an optical laser to heat a deposited gold film and (ii) that it should be possible to perform single-pulse DFXM imaging of the movement of these strain waves at an XFEL, demonstrating the feasibility of this approach.

The new approach outlined in the present work also establishes the pump–probe approach as a potential DFXM experimental modality complementing the real-time imaging experiments performed previously (Dresselhaus-Cooper, 2020; Dresselhaus-Marais *et al.*, 2021). Implementing this approach at XFELs will lead to a nine orders of magnitude improvement in the achievable time resolution down to the femtosecond regime, opening a possibility for studying a large range of both reversible and irreversible phenomena such as phase transformations and damage studies. Furthermore, the approach outlined here is applicable to synchrotron studies with a pulse-width-limited time resolution of 100 ps. This time resolution may introduce motion blur depending on the velocity of moving phase fronts or moving features in the materials. We note that owing to the much lower per-pulse intensity at synchrotrons a stroboscopic acquisition mode would have to be used (Ejdrup *et al.*, 2009). However, this approach will require significant improvements in either the pixel size of gateable photon counting detectors or the magnification provided by the objective optics.

In future experiments, the pump–probe measurement scheme could be combined with scanning the goniometer (ω, ϕ and χ; see Fig. 1) to map out the picosecond-by-picosecond strain-wave-induced dynamics of the strain tensor in three dimensions with sub-micrometre spatial resolution.

To demonstrate the contrast we have relied on two DFXM forward simulation tools (Poulsen *et al.*, 2021; Carlsen & Simons, 2021). This work corroborates the validity of these models, as – although they were constructed independently, using different physical approaches – they arrive at qualitatively similar results. This result provides confidence in the contrast mechanisms proposed and in our approach to planning experiments for the XFEL capabilities. In addition, the comparison illustrates that dynamical effects do not prohibit the visualization of a strain wave. During this work it also became clear that the geometrical-optics code is well suited for optimization purposes as the code runs fast, allowing a rapid exploration of the parameter space. The wave-optics-based simulations, while slower, are superior in terms of their ability to explore dynamical diffraction effects.

The calibration of the DFXM images simulated in this work to the incident beam flux [*i.e.* equation (7)] is approximate at this time, as it neglects factors such as beam polarization, attenuation of beams along optical axes in the X-ray optics, vignetting and quantum efficiency of the detector that can also contribute to the DFXM signal. Perhaps more importantly, positional jitter of the incident beam may reduce intensities. Such positional jitter can be challenging in multiple ways. (i) If a monochromator and/or upstream cleanup slit are introduced, the positional jitter manifests in intensity jitter at the sample because the relevant apertures clip the beam differently as the beam position shifts. (ii) The positional jitter can change the pointing of the beam, altering the incident wavevectors and corresponding diffraction condition, and making it hard to selectively focus on one orientation or lattice spacing. (iii) Sufficient positional jitter can make CRLs prohibitively difficult to align (Breckling *et al.*, 2022).

Having a stable photon energy is also important. If the photon energy or bandwidth jitter, the resulting DFXM beam will sample a different lattice spacing on each shot. Since the self-amplified spontaneous emission beam amplifies regions of the XFEL bandwidth randomly, it shifts the photon energies that determine contrast in DFXM images non-uniformly. This introduces overlaid components of the lattice spacings in a way that is hard to deconvolve when interpreting the results.

On the other hand, the expression for the ratio of intensity being dynamically diffracted may be conservative as the mosaic spread may be smaller locally within the crystal. Moreover, these effects can be readily simulated using the approaches outlined above. Given the count rates of the order of 100 in our simulated images, we conclude that single-pulse visualization of the strain wave with an LCLS-type setup is feasible.

In the XCS setup used for these simulations, the long focal length of the condenser at the beamline (3 m) puts a limit on the beam width. Experiments could overcome this by placing the condenser closer to the sample, facilitating beam heights of a few hundred nanometres. However, to accurately gauge how this affects performance would require simulations beyond the

scope of the present work, as the increased beam divergence affects the depth of focus defining the observation plane.

6. Conclusion

In this work, simulations based on both geometrical optics and wave optics were used to demonstrate the feasibility of DFXM imaging of laser-generated strain waves in diamond single crystals using an XFEL source. Besides showing that these optics formalisms give consistent results, and allowing us to discuss their strengths and weaknesses, these simulations paint an optimistic picture for upcoming experiments at the XCS beamline at LCLS. These experiments, if successful, would constitute a major advancement for DFXM. This would, in turn, open the door for the study of a plethora of ultrafast phenomena, such as, for example, interactions between strain waves and defects (*e.g.* dislocations, twin walls and grain boundaries), rapid material failure, and diffusionless transformations.

Acknowledgements

We are grateful to Bernard Kozioziemski, Eric Folsom, Matthew H. Seaberg, John H. Eggert and Tim van Driel for scientific discussions and technical specifications for the setup at LCLS. We are also very grateful to Daniel Schick for useful discussions, and for developing and maintaining the code (*udkm1Dsim*) used for strain-wave simulations.

Funding information

We are very grateful to our main sponsor, VILLUM FONDEN, which has enabled us to carry out this work through Villum Experiment Grant 00028346. In addition, HFP acknowledges an ERC Advanced Grant, No. 885022, and support from the ESS lighthouse on hard materials in 3D, SOLID, funded by the Danish Agency for Science and Higher Education, grant No. 8144-00002B. Partial contributions from LEDM were performed under the auspices of the US Department of Energy by Lawrence Livermore National Laboratory under contract DE-AC52-07NA27344, and the Lawrence Fellowship.

References

Anthony, T. R., Banholzer, W. F., Fleischer, J. F., Wei, L., Kuo, P. K., Thomas, R. L. & Pryor, R. W. (1990). *Phys. Rev. B*, **42**, 1104–1111.
Breckling, S., Kozioziemski, B., Dresselhaus-Marais, L. E., Gonzalez, A., Williams, A., Simons, H., Chow, P. & Howard, M. (2022). *J. Synchrotron Rad.* Submitted.
Carlsen, M. & Simons, H. (2021). *arXiv*:2106.12412v2 [physics. Comput-ph]. http://arxiv.org/abs/2106.12412.
Clark, J. N., Beitra, L., Xiong, G., Higginbotham, A., Fritz, D. M., Lemke, H. T., Zhu, D., Chollet, M., Williams, G. J., Messerschmidt, M., Abbey, B., Harder, R. J., Korsunsky, A. M., Wark, J. S. & Robinson, I. K. (2013). *Science*, **341**, 56–59.
Cremons, D. R., Plemmons, D. A. & Flannigan, D. J. (2016). *Nat. Commun.* **7**, 11230.
Dresselhaus-Cooper, L. E. (2020). PAL Experimental Report Form LLNL-TR-810542, https://doi.org/10.2172/1630409.
Dresselhaus-Marais, L. E., Winther, G., Howard, M., Gonzalez, A., Breckling, S. R., Yildirim, C., Cook, P. K., Kutsal, M., Simons, H., Detlefs, C., Eggert, J. H. & Poulsen, H. F. (2021). *Sci. Adv.* **7**, eabe8311.
Dutta, B. N. & Dayal, B. (1963). *Phys. Status Solidi B*, **3**, 473–477.
Ejdrup, T., Lemke, H. T., Haldrup, K., Nielsen, T. N., Arms, D. A., Walko, D. A., Miceli, A., Landahl, E. C., Dufresne, E. M. & Nielsen, M. M. (2009). *J. Synchrotron Rad.* **16**, 387–390.
Gonzalez, A., Howard, M., Breckling, S. & Dresselhaus-Marais, L. E. (2020). *arXiv*:2008.04972 [physics. data-an]. http://arxiv.org/abs/2008.04972.
Graebner, J. E. (1996). *Diamond Relat. Mater.* **5**, 1366–1370.
Hatanaka, D., Mahboob, I., Onomitsu, K. & Yamaguchi, H. (2014). *Nat. Nanotechnol.* **9**, 520–524.
Hidnert, P. (1943). *J. Res. Natl Bur. Stand.* **30**, 101–105.
Inoue, I., Tamasaku, K., Osaka, T., Inubushi, Y. & Yabashi, M. (2019). *J. Synchrotron Rad.* **26**, 2050–2054.
Ismail, M. P., Sani, S., Mohd Shofri, F. S. B., Harun, M. & Omar, N. B. (2018). *Mater. Sci. Eng.* **298**, 012025.
Jacobson, P. & Stoupin, S. (2019). *Diamond Relat. Mater.* **97**, 107469.
Jakobsen, A. C., Simons, H., Ludwig, W., Yildirim, C., Leemreize, H., Porz, L., Detlefs, C. & Poulsen, H. F. (2019). *J. Appl. Cryst.* **52**, 122–132.
Jarnac, A., Wang, X., Bengtsson, Å. U. J., Ekström, J. C., Enquist, H., Jurgilaitis, A., Kroon, D., Persson, A. I. H., Pham, V.-T., Tu, C. M. & Larsson, J. (2017). *Struct. Dyn.* **4**, 051102.
Jiang, L. & Tsai, H. L. (2005). *J. Heat Transfer*, **127**, 1167–1173.
Klemens, P. G. & Williams, R. K. (1986). *Int. Mater. Rev.* **31**, 197–215.
Kutsal, M., Bernard, P., Berruyer, G., Cook, P. K., Hino, R., Jakobsen, A. C., Ludwig, W., Ormstrup, J., Roth, T., Simons, H., Smets, K., Sierra, J. X., Wade, J., Wattecamps, P., Yildirim, C., Poulsen, H. F. & Detlefs, C. (2019). *Mater. Sci. Eng.* **580**, 012007.
Larsson, J., Allen, A., Bucksbaum, P. H., Falcone, R. W., Lindenberg, A., Naylor, G., Missalla, T., Reis, D. A., Scheidt, K., Sjögren, A., Sondhauss, P., Wulff, M. & Wark, J. S. (2002). *Appl. Phys. Mater. Sci. Process.* **75**, 467–478.
Lemke, H. T., Breiby, D. W., Ejdrup, T., Hammershøj, P., Cammarata, M., Khakhulin, D., Rusteika, N., Adachi, S. I., Koshihara, S., Kuhlman, T. S., Mariager, S. O., Nielsen, T. N., Wulff, M., Sølling, T. I., Harrit, N., Feidenhans'l, R. & Nielsen, M. M. (2018). *ACS Omega*, **3**, 9929–9933.
Lin, Z., Zhigilei, L. V. & Celli, V. (2008). *Phys. Rev. B*, **77**, 075133.
Lindenberg, A. M., Kang, I., Johnson, S. L., Missalla, T., Heimann, P. A., Chang, Z., Larsson, J., Bucksbaum, P. H., Kapteyn, H. C., Padmore, H. A., Lee, R. W., Wark, J. S. & Falcone, R. W. (2000). *Phys. Rev. Lett.* **84**, 111–114.
Ofori-Okai, B. K., Sivarajah, P., Teo, S. M., Werley, C. A. & Nelson, K. A. (2014). *Proc. SPIE*, **9198**, 919813.
Ormstrup, J., Østergaard, E. V., Detlefs, C., Mathiesen, R. H., Yildirim, C., Kutsal, M., Cook, P. K., Watier, Y., Cosculluela, C. & Simons, H. (2020). *Rev. Sci. Instrum.* **91**, 065103.
Pedersen, A. F., Simons, H., Detlefs, C. & Poulsen, H. F. (2018). *J. Synchrotron Rad.* **25**, 717–728.
Persson, A. I. H., Enquist, H., Jurgilaitis, A., Andreasson, B. P. & Larsson, J. (2015). *J. Appl. Phys.* **118**, 185308.
Porz, L., Klomp, A. J., Fang, X., Li, N., Yildirim, C., Detlefs, C., Bruder, E., Höfling, M., Rheinheimer, W., Patterson, E. A., Gao, P., Durst, K., Nakamura, A., Albe, K., Simons, H. & Rödel, J. (2021). *Mater. Horiz.* **8**, 1528–1537.
Poulsen, H. F., Cook, P. K., Leemreize, H., Pedersen, A. F., Yildirim, C., Kutsal, M., Jakobsen, A. C., Trujillo, J. X., Ormstrup, J. & Detlefs, C. (2018). *J. Appl. Cryst.* **51**, 1428–1436.
Poulsen, H. F., Dresselhaus-Marais, L. E., Carlsen, M. A., Detlefs, C. & Winther, G. (2021). *J. Appl. Cryst.* **54**, 1555–1571.
Poulsen, H. F., Jakobsen, A. C., Simons, H., Ahl, S. R., Cook, P. K. & Detlefs, C. (2017). *J. Appl. Cryst.* **50**, 1441–1456.
Rao, R. R. & Rajput, A. (1979). *Phys. Rev. B*, **19**, 3323–3328.
Schick, D. (2021). *Comput. Phys. Commun.* **266**, 108031.

Schick, D., Bojahr, A., Herzog, M., Shayduk, R., von Korff Schmising, C. & Bargheer, M. (2014). *Comput. Phys. Commun.* **185**, 651–660.
Schultheiß, J., Porz, L., Kodumudi Venkataraman, L., Höfling, M., Yildirim, C., Cook, P., Detlefs, C., Gorfman, S., Rödel, J. & Simons, H. (2021). *Scr. Mater.* **199**, 113878.
Siemens, M. E., Li, Q., Yang, R., Nelson, K. A., Anderson, E. H., Murnane, M. M. & Kapteyn, H. C. (2010). *Nat. Mater.* **9**, 26–30.
Simons, H., Ahl, S. R., Poulsen, H. F. & Detlefs, C. (2017). *J. Synchrotron Rad.* **24**, 392–401.
Simons, H., Haugen, A. B., Jakobsen, A. C., Schmidt, S., Stöhr, F., Majkut, M., Detlefs, C., Daniels, J. E., Damjanovic, D. & Poulsen, H. F. (2018). *Nat. Mater.* **17**, 814–819.
Simons, H., Jakobsen, A. C., Ahl, S. R., Detlefs, C. & Poulsen, H. F. (2016). *MRS Bull.* **41**, 454–459.
Simons, H., King, A., Ludwig, W., Detlefs, C., Pantleon, W., Schmidt, S., Stöhr, F., Snigireva, I., Snigirev, A. & Poulsen, H. F. (2015). *Nat. Commun.* **6**, 6098.
Snigirev, A., Kohn, V., Snigireva, I. & Lengeler, B. (1996). *Nature*, **384**, 49–51.
Starikov, A. & Wolf, E. (1982). *J. Opt. Soc. Am.* **72**, 923–928.
Takagi, S. (1962). *Acta Cryst.* **15**, 1311–1312.
Tzou, D. Y., Chen, J. K. & Beraun, J. E. (2002). *Int. J. Heat Mass Transfer*, **45**, 3369–3382.
Victor, A. C. (1962). *J. Chem. Phys.* **36**, 1903–1911.
Wang, S. F., Hsu, Y. F., Pu, J. C., Sung, J. C. & Hwa, L. G. (2004). *Mater. Chem. Phys.* **85**, 432–437.
Wang, Y., Lu, Z. & Ruan, X. (2016). *J. Appl. Phys.* **119**, 225109.
Wen, H., Cherukara, M. J. & Holt, M. V. (2019). *Annu. Rev. Mater. Res.* **49**, 389–415.
Wolfe, J. P. & Hauser, M. R. (1995). *Ann. Phys.* **507**, 99–126.
Yildirim, C., Cook, P., Detlefs, C., Simons, H. & Poulsen, H. F. (2020). *MRS Bull.* **45**, 277–282.
Zaretsky, E. B. (2008). *J. Appl. Phys.* **104**, 123505.